

A Method for Identifying Kolmogorov's Inertial Subrange in the Velocity Variance Spectrum

DAVID G. ORTIZ-SUSLOW, QING WANG, JOHN KALOGIROS,^a AND RYAN YAMAGUCHI

Department of Meteorology, Naval Postgraduate School, Monterey, California

(Manuscript received 18 February 2019, in final form 2 August 2019)

ABSTRACT

Kolmogorov's inertial subrange is one of the most recognized concepts in fluid turbulence. However, the practical application of this theory to turbulent flows requires identifying subrange bandwidth. In the atmospheric boundary layer, decades of investigation support Kolmogorov's theory, but the techniques used to identify the subrange vary and no systematic approach has emerged. The algorithm for robust identification of the inertial subrange (ARIIS) has been developed to facilitate empirical studies of the turbulence cascade. ARIIS systematically and robustly identifies the most probable subrange bandwidth in a given velocity variance spectrum. The algorithm is a novel approach in that it directly uses the expected 3/4 ratio between streamwise and transverse velocity components to locate the onset and extent of the inertial subrange within a single energy density spectrum. Furthermore, ARIIS does not assume a $-5/3$ power law but instead uses a robust, iterative statistical fitting technique to derive the slope over the identified range. This algorithm was tested using a comprehensive micrometeorological dataset obtained from the *Floating Instrument Platform (FLIP)*. The analysis revealed substantial variation in the inertial subrange bandwidth and spectral slope, which may be driven, in part, by mechanical wind-wave interactions. Although demonstrated using marine atmospheric data, ARIIS is a general approach that can be used to study the energy cascade in other turbulent flows.

1. Introduction

Nearly 80 years ago, Kolmogorov proposed a set of theories that described a universal structure of small-scale turbulent motion within a homogeneous fluid under high Reynolds numbers (Re ; Batchelor 1947, 1953). These theories have been applied to the experimental study of fluid turbulence across a wide range of flows, from the laboratory to geophysical scale. The atmospheric surface layer (ASL) is considered to be at sufficient Re to develop the turbulence structure Kolmogorov identified. Following the original publication (Kolmogorov 1941b,a) various studies corroborated his theories, thereby establishing a general acceptance of their validity within the atmosphere (MacCready

1962; Miyake et al. 1970; Atta and Chen 1970; Kaimal et al. 1972).

One of the applications of Kolmogorov's theories on the study of the ASL is the use of the inertial dissipation method (IDM) to estimate the momentum flux, as well as the rate of turbulence kinetic energy (TKE) dissipation (ε) near the surface (e.g., Large and Pond 1981, 1982; Fairall and Larsen 1986). From the assumptions that Kolmogorov made to develop his theories, dimensional analysis yields the TKE spectral density over the inertial subrange:

$$E(k) = \alpha \varepsilon^{2/3} k^{-5/3}, \quad (1)$$

which has become one of the most widely recognized equations in the study of geophysical fluid turbulence; α is a universal proportionality constant (Yaglom 1981; Deacon 1988; Hogstrom 1996; Yeung and Zhou 1997) and k is wavenumber. The spectrum represents the inviscid cascade mechanism (Onsager 1945) from the energy-containing eddies to the dissipation spectrum (Tennekes and Lumley 1972). Assuming one can measure $E(k)$, an estimate of ε may be derived, which in turn can be related to the friction

 Denotes content that is immediately available upon publication as open access.

^a Additional affiliation: National Observatory of Athens, Athens, Greece.

Corresponding author: Qing Wang, qwang@nps.edu

(or shear) velocity u_* . Following [Yelland and Taylor \(1996\)](#),

$$\varepsilon = \frac{u_*^3}{\kappa z} \phi_\varepsilon, \quad (2)$$

where κ is the von Kármán constant, z is the altitude within the surface layer, and ϕ_ε is the nondimensional dissipation function from Monin–Obukhov similarity theory. The ϕ_ε is a function of stability, $\zeta = z/L$ (L is the Obukhov length), and must be determined empirically (e.g., [Large and Pond 1981](#); [Yelland and Taylor 1996](#)). A corollary can be made in the ocean where the same formulas are applied to investigating developed turbulence in stable boundary layers and the dependence on the Dougherty–Ozmidov length scale ([Grachev et al. 2015](#)).

Operationally, IDM is advantageous because it is usually evaluated over a subrange of k for which the influence of platform motion, flow distortion, and surface gravity waves (in the case of the marine environment) are negligible. However, IDM remains an *indirect* method, and the advent of higher-quality and cost-effective motion systems has promoted the eddy covariance technique for deriving flux estimates ([Edson et al. 2013](#)). Despite this, IDM persists as a viable method with continued application in both field and numerical studies ([Jabbari et al. 2015](#); [Hackerott et al. 2017](#)).

One practical challenge to using IDM is determining the appropriate subrange of k . Kolmogorov did not provide explicitly for identifying the appropriate subrange and, while Eq. (1) is expected to be widely valid, the bandwidth of k (Δk) over which it applies depends on Re ([Batchelor 1953](#); [Tennekes and Lumley 1972](#)). In reviewing the ASL literature, a sample of prominent and recent studies revealed no consistent method or approach for identifying Δk in observational data ([Payne and Lumley 1966](#); [Miyake et al. 1970](#); [Kaimal et al. 1972](#); [Kaimal 1978](#); [Large and Pond 1981, 1982](#); [Fairall and Larsen 1986](#); [Edson et al. 1991](#); [Durand et al. 1991](#); [Anderson 1993](#); [Yelland and Taylor 1996](#); [Edson and Fairall 1998](#); [Sjöblom and Smedman 2002](#); [Hackerott et al. 2017](#); [Muñoz-Esparza et al. 2018](#)). In fact, only three of those listed here directly state what bandwidth was used and how it was determined. [Yelland and Taylor \(1996\)](#) and [Muñoz-Esparza et al. \(2018\)](#) both used fixed bandwidths for the inertial subrange from 2 to 4 Hz and from 0.5 to 10 Hz, respectively, with no reported justification. [Sjöblom and Smedman \(2002\)](#) reported that they visually inspected their spectra and rejected those that did not appear to follow a $-5/3$ slope. As an oceanic turbulence example, [Grachev et al. \(2015\)](#) derived estimates for ε using IDM over a fixed

bandwidth [0.49, 0.74] Hz, which they determined to be within the inertial subrange. Across studies over land and ocean, the most common approach to identifying the inertial subrange, or validating its presence, was visually comparing the measurement-derived power spectrum with a line exhibiting a logarithmically (log) scaled slope of $-5/3$. In addition, it was rare for investigators to give any indication of the prevalence of an inertial subrange in their aggregate dataset or any sense of the relative uncertainty they had in their identified bandwidth and its spectral properties. Although this may not have been critical to the ultimate findings reported in all of the studies listed above, it highlights an approach across decades of study that is highly idiosyncratic and reflects some of the most highly cited studies on the subject (aggregate Google Scholar citations > 7500).

[Hackerott et al. \(2016\)](#) recently presented an iterative, inertial subrange detection method (see the appendix of that paper). The underlying basis of the method was to find the Δk where α converges, to within $\pm 10\%$ of 1 standard deviation. This algorithm is more robust than visual inspection and indirectly relies on Kolmogorov's underlying assumption of isotropy (discussed further below). However, the [Hackerott et al. \(2016\)](#) method relies on an estimate of ε (via polynomial fitting of the log-linear portion of the spectrum) and the universality of the $-5/3$ power law. A similar method was employed by [Jabbari et al. \(2015\)](#) to study simulations of open channel flow. While methods like this exist in the physics literature, in the context of the ASL, techniques appear to be ad hoc, and the documentation of what specifically was done is not consistently reported. Furthermore, visual inspection persists as a credible means for identifying Kolmogorov's inertial subrange within a given spectrum.

Here, it is argued that the lack of a consistent or efficient technique for detecting the inertial subrange in observed or modeled turbulence spectra presents a significant oversight in the meteorological community. To address this situation, the “algorithm for robust identification of the inertial subrange” (ARIIS) was developed. Although the idea of devising a technique to locate the inertial subrange is not novel, having been necessary since the theory's 1941 proposal, there is a need for a standard approach that can be easily incorporated into any investigator's analytical toolbox. This is akin to the way certain eddy covariance flux algorithms have become conventional and have been widely utilized in studying a diversity of ASL datasets (e.g., COARE). The primary objective of ARIIS is to move away from an overreliance on the *eyeball* test as a valid assessment for the presence and location of Kolmogorov's inertial subrange. The scope of this article will be to detail the basis and implementation of

ARIIS, using a field dataset collected from the *Floating Instrument Platform (FLIP)* as an example. Some analysis of the results from *FLIP* will also be discussed, but the in-depth analyses exploring this particular dataset have been summarized in a separate article by the authors that is currently in the peer-review process, as well as being the focus of ongoing investigation.

2. Kolmogorov's inertial subrange

The basis for Eq. (1) will be outlined below, and, unless otherwise noted, the source of this review comes from Batchelor (1953) and Tennekes and Lumley (1972). The former is based largely on one of the first English translations of the original articles published in Russian (see Batchelor 1947). This work will only focus on Kolmogorov's formulas as they relate to the velocity variance spectrum.

Given a homogeneous and incompressible fluid at sufficiently high Re , a portion of the total turbulent energy spectrum can be considered in equilibrium with local conditions and is thus independent of the mean. If all of the inertial input at low k is dissipated by viscosity (ν) at high k , then the energy across this equilibrium spectrum is functionally defined as

$$E = E(k, \varepsilon, \nu). \quad (3)$$

Since Eq. (3) is independent of the mean variance, this relationship should be valid for any flow and formulaically summarizes *universal equilibrium theory*.

Dimensional analysis of E yields one possible result,

$$E = \nu^{5/4} \varepsilon^{1/4} f(k\eta), \quad (4)$$

where the Kolmogorov microscale, $\eta = (\nu^3/\varepsilon)^{1/4}$, is the upper limit of k in Eq. (4). The eddies across E are also characterized by the Kolmogorov velocity scale, $v = (\nu\varepsilon)^{1/4}$ so that Eq. (4) can be written as

$$E = v^2 \eta f(k\eta). \quad (5)$$

Therefore, to predict $E(k)$, one must determine the form of $f(k\eta)$, which may be complicated. However, Kolmogorov argued that as Re continued to increase [beyond the cutoff for Eq. (3) to be valid] a subrange of E will develop in which the influence of both the mean and ν could be neglected. This inviscid portion of E would then be solely controlled by ε and thus considered to be an *inertial subrange*. Assuming a power law in Eq. (4),

$$\begin{aligned} E &\sim \nu^{5/4} \varepsilon^{1/4} f(k\nu^{3/4} \varepsilon^{-1/4}) \\ &\sim \nu^{5/4} \varepsilon^{1/4} (k \nu^{3/4} \varepsilon^{-1/4})^\delta, \end{aligned} \quad (6)$$

it can be seen that, to eliminate viscosity from E , δ must have the value

$$\begin{aligned} 1 &= \nu^{5/4} \nu^{3\delta/4}, \\ \nu^{-5/4} &= \nu^{3\delta/4}, \\ -5/4 &= 3\delta/4, \\ \delta &= -5/3. \end{aligned} \quad (7)$$

Substituting this δ into Eq. (6), we arrive again at Eq. (1),

$$E(k) = \alpha \varepsilon^{2/3} k^{-5/3}, \quad (8)$$

which will be referred to as Kolmogorov's spectrum or the inertial subrange spectrum. The k dependence of this spectrum will be referred to as either the power law or inertial subrange slope. This relation is only valid over a specific subrange, or bandwidth Δk , for which $E(\Delta k)$ satisfies these conditions:

- 1) $E(\Delta k)$ is isotropic over Δk and
- 2) $E(\Delta k)$ exhibits a $-5/3$ dependence on k .

Both of these conditions must be simultaneously true for Kolmogorov's spectrum to be valid (Yeung and Zhou 1997).

To emphasize, a subrange within any spectrum exhibiting $k^{-5/3}$ does not necessarily signify that that portion is the inertial subrange, or even signify the presence of the inertial subrange anywhere within the total spectral bandwidth. The condition of isotropy must be satisfied because of Kolmogorov's original argument that the turbulent motions over this subrange are independent from the inherently anisotropic mean inertial motions (Tennekes and Lumley 1972). The second condition may appear circular, but it underscores that the $-5/3$ power law is the only possible, dimensionally consistent outcome for Eq. (4), assuming an inviscid cascade from low to high k . Therefore, condition 1 may be considered the more fundamental of the two, since it is based on the truly fluid mechanical idea of a homogeneous, high Re flow in equilibrium.

The E in Eq. (4) is the total TKE spectrum, which can be related to the one-dimensional velocity variance spectrum, $S_{\beta\beta}(k) = a_\beta E(k)$. For the purposes of this paper, β can be the streamwise (u), horizontal transverse (v), or vertical (w) velocity components. Over the inertial subrange, there is a predictable relationship between S_{uu} and $S_{vw,ww}$:

$$S_{uu} = (3/4)S_{vw,ww}, \quad (9)$$

and therefore an isotropy coefficient \mathcal{I} can be defined (Jimenez et al. 1992),

$$\mathcal{I}(k) = \frac{S_{uu} - k\partial S_{uu}/\partial k}{2S_{vv,ww}}, \quad (10)$$

such that $\mathcal{I}(\Delta k) \rightarrow 1$.

Typical ASL turbulence studies derive $S_{\beta\beta}$ from high-temporal-resolution anemometry. Therefore, turbulence is not resolved in terms of k but rather frequency n . The transformation from spatial to temporal scale requires invoking Taylor's frozen turbulence theory, which allows $k = 2\pi n/U$, where U is the mean advection velocity. Utilizing n versus k does not result in any fundamental change to the Kolmogorov spectrum or its implications and so the inertial subrange frequency bandwidth can be defined as Δn . Note that there is some controversy with how to properly apply Taylor's theory (e.g., Wyngaard and Clifford 1977) to account for a frequency-independent offset [Edson and Fairall (1998) report a $\sim 2\%$ change in spectral amplitude], but this is not as critical here since the primary focus is for the slope of $S_{\beta\beta}(n)$, which should not be effected by this correction.

In the ASL, some anisotropy is expected (Wyngaard 2010) and has been observed using sonic anemometry for the case of thermodynamically stable and heterogeneous conditions (Babić and Rotach 2018). In this previous work, it was found that in fact $S_{uu}/S_{vv} \neq S_{uu}/S_{ww}$, with the left-hand side being $> 3/4$. This was observed using three-dimensional sonic anemometers (Gill Instruments, Ltd., WindMaster Pro) and created uncertainty in the authors' estimates of ε . Although this previous work was in a unique regime (i.e., stable conditions and canopy fetch), these interesting findings suggest that examining $\mathcal{I}(n)$ in all dimensions may be important to characterizing the high-frequency turbulence.

3. Field dataset

The data used to develop and test ARIIS were collected as part of the Coupled Air–Sea Processes and Electromagnetic Ducting Research (CASPER) West Coast field campaign (CASPER-West) that took place south of the Channel Islands, offshore of Southern California, in September and October of 2017 (Fig. 1). CASPER, as a whole, focused on understanding how variability within the marine atmospheric boundary layer (MABL) affects the propagation of electromagnetic and electro-optical radiation over the ocean (Wang et al. 2018). CASPER-West was an intensive air–sea interaction study in which coordinated measurements were made from a variety of research vessels and platforms.

This included the Research Vessel *Sally Ride*, *FLIP*, a suite of autonomous ocean gliders, and shore-based measurement systems as well as the network of Coastal Data Information Program/National Data Buoy Center oceanographic/meteorological surface buoys that are stationed in the Southern California Bight region. This study will focus on the atmospheric measurements made from a mast installed on the port boom of *FLIP* (Fig. 1).

FLIP is a 108-m-long spar buoy that uses water-filled ballast tanks to stay vertical at the ocean surface (Fisher and Spiess 1963). For CASPER-West, *FLIP* was trimoored, which resulted in a natural vertical and azimuthal oscillation with period 63.38 s; a subharmonic was also present at approximately 33 s. These motions were persistent, but their absolute deviations were ~ 1 – 10 cm, which is significantly less than the motion experienced on a typical research vessel, even under mild or moderate conditions. For this reason, *FLIP* remains one of the best platforms for making undisturbed oceanographic and atmospheric measurements near the interface in a wide variety of environmental states.

FLIP is outfitted with booms that enable measurements to be made far away from platform's superstructure. The port-side boom is approximately 18 m long and extends perpendicular from the main body (see Fig. 1). At the end of the boom a 13-m-long meteorological mast, of aluminum triangular lattice, was emplaced and installed with a total of 17 atmospheric measurement levels. Across these levels, was arranged overlapping bulk and turbulence-resolving profiles, which included: combined 17 two- or three-dimensional (3D) sonic anemometers, 20 relative humidity probes, and 25 bulk temperature probes. The measurement capability of this mast represents an extensive characterization of the marine ASL (MASL) during CASPER-West and one of the most complete near-surface atmospheric profile datasets collected over the ocean to date. The port boom was also outfitted with atmospheric pressure sensors, an inertial motion unit (IMU) paired with each 3D sonic anemometer, a laser altimeter (for instantaneous wave height under the boom), and a differential global positioning system (DGPS) antenna array for location and non-magnetometer-derived heading.

This study presents analysis of the turbulence-resolving, or flux, measurements from multiple levels (i.e., profile) from the mast. The flux profile was composed of seven 3D sonic anemometers, given in order of height above the ocean: one 3D R. M. Young Co. 81000 (3 m); a Campbell Scientific, Inc., CSAT3/LiCOR LI7500 infrared gas analyzer combination (4 m); and five Campbell Scientific "IRGASON" systems

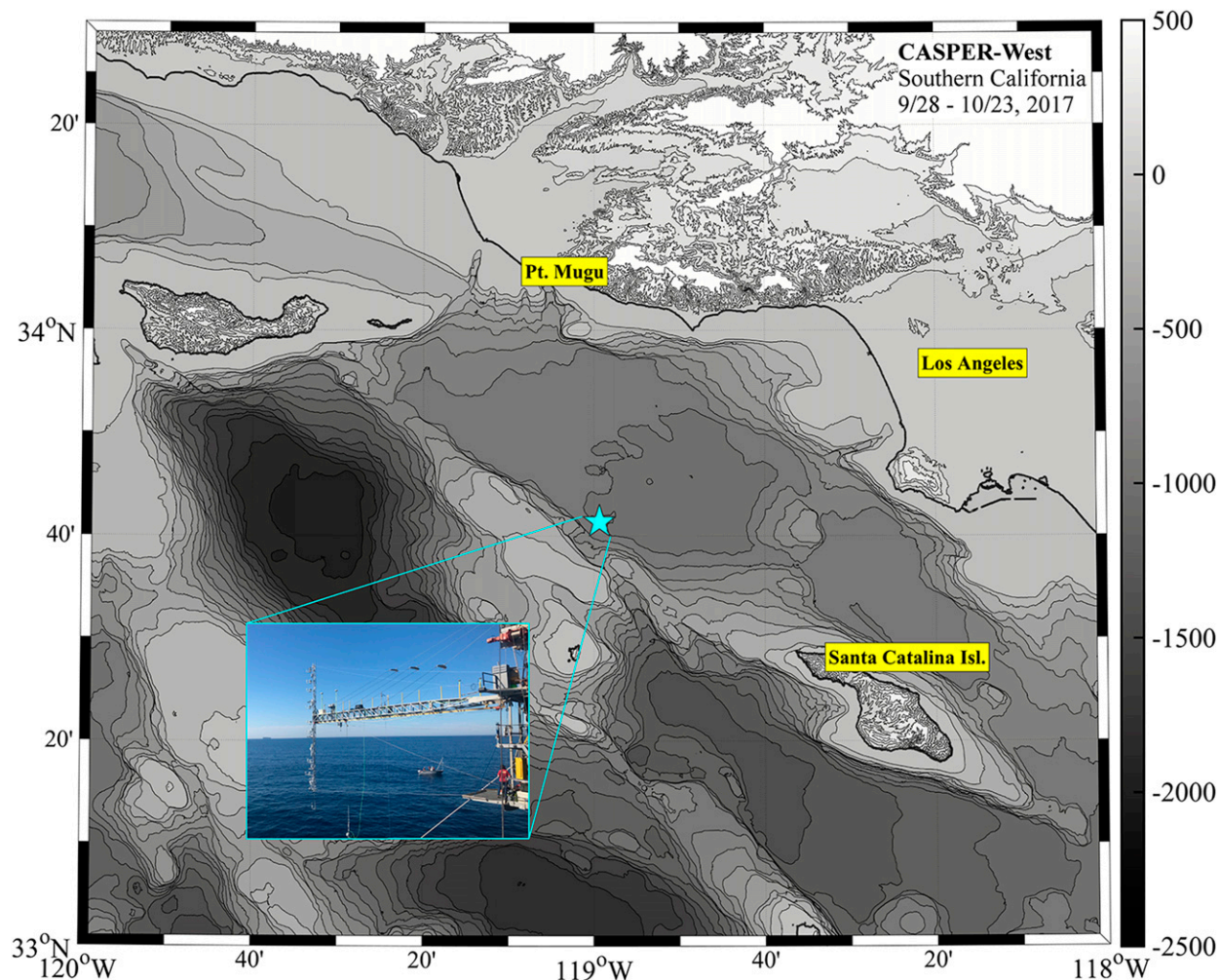


FIG. 1. The location of the CASPER-West field campaign, with the location of *FLIP* marked by a star. The inset shows the port boom and meteorological mast. *FLIP*'s mean heading was $\sim 290^\circ$ from true north.

(5–16 m)—heights are approximate. The exact altitude above sea level depended on various factors impacting *FLIP* displacement and was recorded using the laser altimeter. The upper six levels resolved the momentum and total heat flux, the R. M. Young only resolves the momentum and sensible heat flux. The datalogger sampling rate of the IRGASONS was set to 50 Hz, and the other two 3D anemometers were sampled at 20 Hz.

For the IRGASONS, there are two major caveats to their configuration that must be addressed here. First, a 50-Hz datalogger scanning rate is suboptimal for minimizing the timing jitter associated with our noninteger divisor scanning rate relative to the 60-Hz chopper motor that is intrinsic to the IRGASON, per the postexperiment guidance we received from the manufacturer Campbell Scientific. The chopper-motor frequency is governed by the synchronization of the anemometry and hygrometry that is key to the design

of the IRGASON system; therefore, Campbell Scientific strongly recommends using an integer divisor as a datalogger scanning rate (e.g., 10 or 20 Hz). However, this point is not made explicitly clear in the IRGASON documentation, if an investigator is not using the native acquisition software—at the time of writing, as a result of our discussions with Campbell Scientific there is an intention to amend the instrument manual. Second, to reduce the effect of aliasing and noise, an internal 20-Hz low-pass filter is applied to the raw data stream. The second caveat is easily visible by inspecting the raw power spectrum of any IRGASON wind component. Because of the filter design, all of the spectra analyzed for this study were truncated to frequencies below 16 Hz. A thorough postexperiment investigation, using a simulated signal, sampled in the exact way the CASPER-West IRGASONS were set up, was conducted to determine the potential impact of the timing

jitter on the CASPER-West data. The results indicated that the combined effect of jitter (from our sampling configuration) and aliasing (inherent to the system) decreases the precision of individual, high-frequency spectral components, which results in a positive bias in the mean spectral slope at frequencies above 20 Hz (the simulations did *not* apply the low-pass filter). Furthermore, the spectral uncertainty introduced by these effects is on the order of a few percent, which may be very small relative to the operational uncertainty of the observational data. The small magnitude of this effect, combined with its restriction to frequencies above 20 Hz, gives us confidence that this suboptimal data sampling configuration does not have a discernible impact on the results and analysis presented here. However, future IRGASON deployments should adhere to Campbell Scientific's guidance on the optimal sampling configuration.

Collocated with each flux level (except the R. M. Young) was a VectorNav Technologies, LLC, IMU (VN-100), that resolved the linear and rotational accelerations for each level of the mast at 50 Hz. The DGPS on the port boom was capable of precisely measuring the true heading of *FLIP* without using a magnetometer, which could be affected by the ferrous superstructure. The IMU and DGPS were blended at the high and low frequencies, respectively, and then used to motion correct the raw anemometer velocities following Edson et al. (1998). Before motion correction, the raw velocity data were screened for spurious samples using either internal diagnostics (for the IRGASONS) or a 20-sample-wide, moving median absolute deviation (MAD) filter. This approach is similar to some of the techniques described in the thorough, outlier-detection review given by Starkenburg et al. (2016) and that were determined to be the most reliable and stable. Any particular processing window in which over 10% of the samples were flagged in the screening was excised from the final dataset. Outlier samples in the preserved records were removed, and the gap was interpolated using a linear polynomial. Further details on the instrument systems deployed and the data quality control and assessment of the CASPER-West measurements are provided in Ortiz-Suslow et al. (2019), which also contains a detailed review and analysis of the motion of *FLIP* during CASPER-West and how this compares with previous *FLIP* studies.

Figure 2 highlights the general MASL conditions experienced during CASPER-West. The focus here will be on the period from 30 September to 23 October UTC. These conditions were typical of the autumnal Southern California coastal region. Daily variability was characterized by low, generally easterly wind in the local

morning and a transition to a sea breeze in the local afternoon, $U \approx 5 \text{ m s}^{-1}$. The MASL was typically unstable, with a median \pm MAD of $\zeta = -0.319 \pm 1.875$. The time record also experienced three Santa Ana wind events, characterized by stratified conditions ($\zeta > 0$), and the passage of a strong westerly front (20–21 October) during which sustained wind speeds exceeded 10 m s^{-1} for approximately 24 h.

4. ARIIS

The primary aim in developing ARIIS was to efficiently and robustly identify the most probable Δn in an observed velocity variance spectrum. It is important to note that Kolmogorov's inertial subrange is a theoretical construct, and therefore its wavenumber (or frequency) range in a variance spectrum must be empirically identified—hence the challenge to investigators for 80 years. In fact, this explains the existence of various techniques for detecting the subrange and why visual inspection remains acceptable. ARIIS is essentially a series of systematic steps that are executed to determine the most probable Δn in the given turbulence spectrum.

a. The observed turbulence spectra

To develop ARIIS, the motion-corrected *FLIP* flux profile data were processed in 30-min windows, with 50% overlap. Over this interval, records were rejected if the mean wind direction θ_z was within the $\sim 150^\circ$ sector determined to be heavily influenced by flow distortion around the platform [see Ortiz-Suslow et al. (2019) for a full analysis]. This sector generally corresponds to winds with an easterly component, given *FLIP*'s mean heading of $290^\circ \pm 6.3^\circ$. The autovariance spectra were calculated for each 30-min window using the detrended velocity record, a four-term Blackman–Harris window, and the MATLAB software package's fast Fourier transform (FFT). Before starting the identification algorithm, the individual spectra were smoothed using a logarithmically uniform bin average with 103 discrete bins (91 used for the lowest two levels because of lower sampling frequency).

The observed autovariance wind spectrum can be normalized into natural, or surface layer, coordinates in order to account for the expected dependence on wind forcing and height into the turbulent, wall-bounded layer (Miyake et al. 1970; Kaimal et al. 1972). Using the natural frequency, $f = nz/U$, the normalized 1D variance spectra derived from Eq. (1) are

$$F_{uu} = \frac{nS_{uu}}{u_*^2} = \alpha_u \left(\frac{\kappa z \varepsilon}{u_*^3} \right)^{2/3} \left(\frac{nz}{U} \right)^{m_{uu}} = \alpha_u \phi_\varepsilon f^{m_{uu}} \quad \text{and} \quad (11)$$

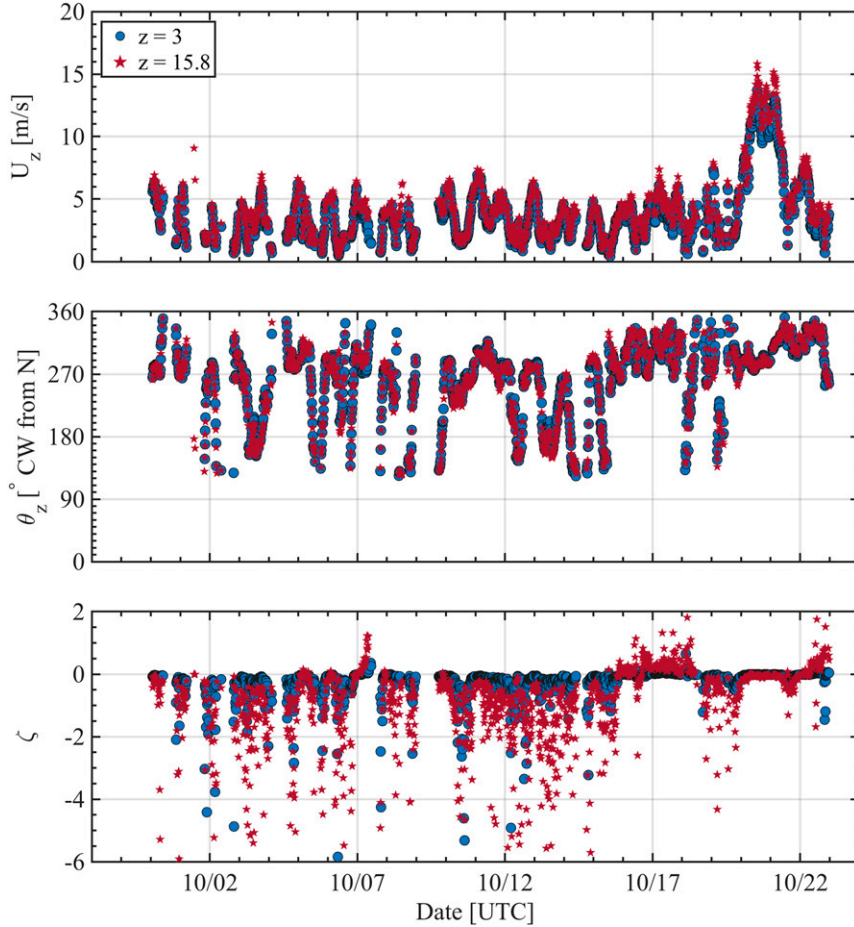


FIG. 2. Times series of 30-min mean (top) wind speed U_z and (middle) direction θ_z , as well as (bottom) atmospheric stability ζ over the CASPER-West study period. Only the data that were passed onto ARIIS are shown. Wind speed U_z was not corrected for nonneutral stability and represents the mean at height z .

$$F_{\beta\beta} = \frac{nS_{\beta\beta}}{\sigma_w^2} = \alpha_\beta \left(\frac{\kappa z \varepsilon}{u_*^3} \right)^{2/3} \left(\frac{nz}{U} \right)^{m_{\beta\beta}} = \alpha_\beta \phi_\varepsilon f^{m_{\beta\beta}}, \quad (12)$$

where $\alpha_{u,\beta}$ are component-wise, scaled versions of α , σ_w^2 is the vertical velocity variance, and the dimensionless TKE dissipation rate ϕ_ε is used. At high f , F_{uu} and $F_{\beta\beta}$ should collapse onto a common slope over the inertial subrange (with slope $-2/3$, herein referred to as m_0) and separations at low f should be controlled by ζ . This was well documented in the seminal surface-layer study of Kaimal et al. (1972). Inspections of the CASPER-West data (not shown here) revealed a similar pattern as expected over low f , but with significantly more separation in the ζ -segregated spectra over high f than would be expected on the basis of Kaimal et al.'s work (their Figs. 3 and 4). During the general data inspections of CASPER-West, this unexpected behavior, which was observed to varying degrees across

the entire profile, indicated potential for actual variability in the inertial subrange and motivated the development of ARIIS.

b. The algorithm

The first step in ARIIS is to locate the inertial subrange bandwidth Δf . This was done automatically by relying on the first condition for Kolmogorov's theory, namely that Δf must occur over the isotropic portion of the spectrum. Equation (10) gives the isotropy coefficient, but programmatically it was simpler to define the isotropic ratio,

$$\mathcal{R}(n) = S_{uu}/S_{ww}, \quad (13)$$

without losing any generality. The $S_{\beta\beta}$ have been smoothed but are not scaled using surface-layer coordinates. Over the isotropic bandwidth, $\mathcal{R}(n)$ converges

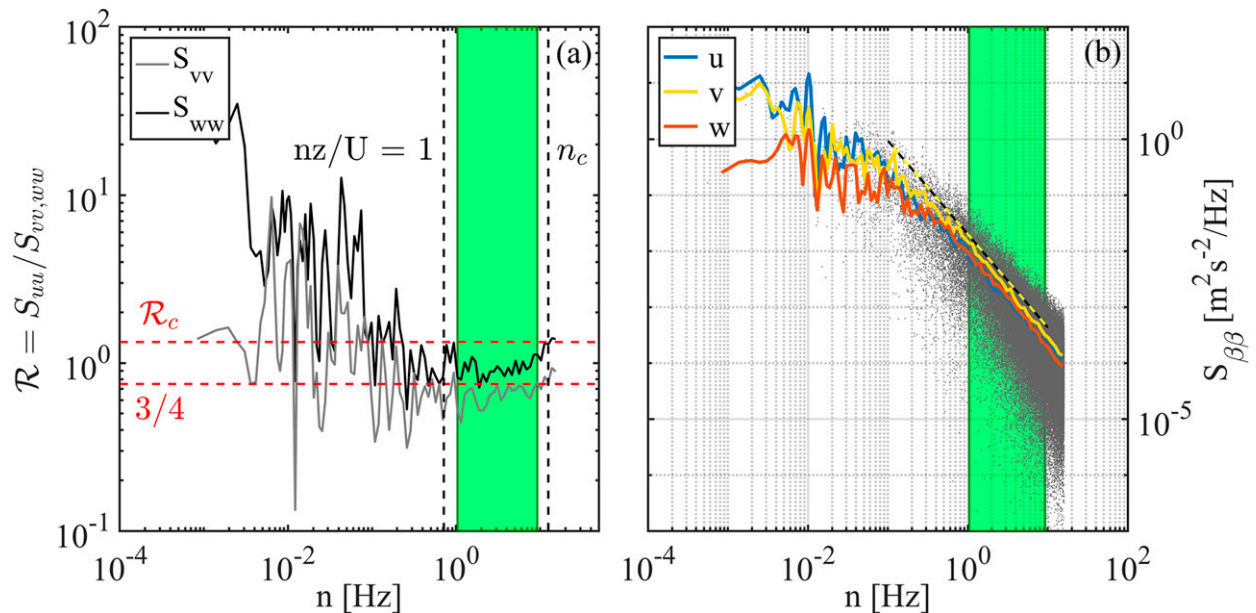


FIG. 3. An example of ARIIS-identified inertial subrange. (a) The vertical dashed lines mark the low-frequency limit and high-frequency limit (n_c could be n_{Nyq}) from ARIIS. The horizontal red dashed lines mark \mathcal{R}_c (4/3) and the expected isotropic value (3/4). (b) The velocity variance spectra for this example, with Kolmogorov's $-5/3$ slope (the black and yellow dashed line). The shaded green bandwidth is the inner 80% passed on as the inertial subrange Δn . This sample comes from $z = 8.46$ m at 0130 UTC 30 Sep. The mean U_z and θ_z were 6.04 m s^{-1} and 278.2° , respectively.

on $3/4$ (Tennekes and Lumley 1972) and so a criteria-based test can be made to find the continuous range of n over which $\mathcal{R}(n) \approx 3/4$. It is noted that \mathcal{R} and \mathcal{I} are physically equivalent. The use of S_{ww} , instead of S_{vv} , in this ratio can be justified by the fact that S_{ww} in the surface layer reveals an inertial subrange and collapses into a narrow band independent of atmospheric stability at higher frequencies than S_{vv} , especially under stable atmospheric conditions (Kaimal et al. 1972).

This approach was applied by searching from low to high n and finding the continuous subrange where $\mathcal{R}(n) < \mathcal{R}_c$ (i.e., the critical value for sufficiently isotropic), where the limits of Δn had to satisfy this condition: $U/z < n < n_{Nyq}$, where n_{Nyq} is the Nyquist sampling frequency (given the caveats noted above, the value for n_{Nyq} would be the maximum frequency of the truncated spectrum). The lower limit of n comes from the physical constraint on the turbulent eddies that can be resolved and that are not expected to be significantly distorted by the surface ($f \geq 1$). Typically, $f \geq 1$ is used as the onset of the inertial subrange, but ARIIS estimates the actual initiation frequency of the subrange, with U/z as the lowest possible limit. This makes ARIIS a unique and more general approach relative to other techniques, which use either visual inspection (e.g., Sjöblom and Smedman 2002) or arbitrary limits (e.g., Yelland and Taylor 1996), without accounting for the $\mathcal{R}(n)$.

For CASPER-West, if $U/z \leq 1/3 \text{ s}^{-1}$, then the lower limit of Δn was set to 0.333 Hz , to avoid surface gravity wave band contamination. Also, specific to CASPER-West, $\mathcal{R}_c = 4/3$, which is a very generous cutoff that was determined by inspecting the output of ARIIS. If the final number of bins in Δn was < 4 , the spectra were rejected from the final dataset (i.e., no Δn found). As a further precaution, only an inner fraction of n bins was passed on as Δn (here 80% was chosen). The results of this process for an example spectrum are given in Fig. 3.

After identifying Δn , ARIIS uses an iterative fitting algorithm to estimate the power law over the located subrange. This step is fundamentally different from previously published methods on detecting the inertial subrange because ARIIS does not assume that the isotropic bandwidth follows a $-5/3$ power law. The $F_{\beta\beta}$ can be statistically represented using a log-scaled linear relation:

$$\log(F_{\beta\beta}) = A + m_{\beta\beta} \times \log(f), \quad (14)$$

where A and $m_{\beta\beta}$ can be determined through least squares regression. Note that $m_{\beta\beta}$ is expected to be m_0 but is allowed to vary freely. The regression process enables calculating an independent measure of the uncertainty (μ) for $m_{\beta\beta}$ based on the residual (δ) between the observed $F_{\beta\beta}$ and the linear

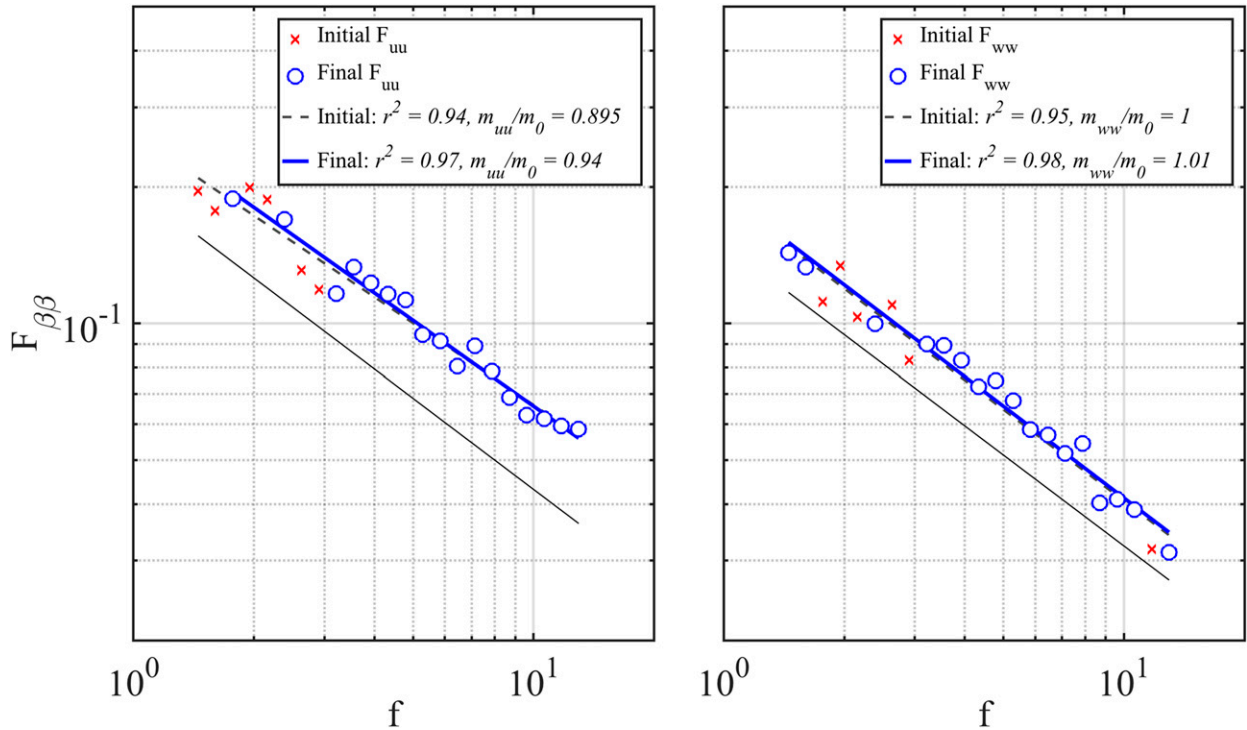


FIG. 4. An example of the robust fitting technique applied by ARIIS to the (left) u and (right) w wind components, using the example spectra from Fig. 3. The solid black line has a log–log slope of $-5/3$.

model. The μ is a standard error estimate and is defined as

$$\mu \equiv \left\{ \left(\delta^2 \sum_{i=1}^N f^2 \right) / [(N - 2)N\sigma^2] \right\}^{1/2},$$

where $\delta^2/(N - 2)$ is known as the mean square error and σ^2 is the total variance in $F_{\beta\beta}$. The f^2 is the sum of squares of $\log(f)$, and N is the number of discrete bins in Δn .

A four-step robust fitting technique was used to determine $m_{\beta\beta}$: 1) log-scaled linear regression was executed over Δf ; 2) the Cook’s distance D was determined for each fitted amplitude; 3) any amplitude where $D > D_{\text{threshold}}$ was removed; and 4) the final regression was rerun using the filtered spectra. The D may be defined as an indication of the influence a single sample has on the overall regression. In this way, D may be used to identify outliers without relying on dependent statistics such as the mean, median, or variance. This metric was defined as

$$D(i) = \frac{\sum_{j=1}^N [y_j - y_{j(i)}]^2}{p \times \text{MSE}}, \quad (15)$$

where p is the number of predictor coefficients in the regression (here, $p = 1$), MSE is the mean square

error between the observed values and the original fitted response y_j , and $y_{j(i)}$ is the fitted response excluding sample i . In other words, D is calculated by iteratively fitting the observations, excluding observation i . Chatterjee and Hadi (1988) suggest a $D_{\text{threshold}} = 4/(N - p - 1)$ for samples with too much influence. The regression steps were completed independently for all $F_{\beta\beta}$; thus each component can exhibit a different power law over Δf . Spectra with $N < 3$ after the Cook’s distance algorithm were removed from the final dataset (this was rare).

We emphasize that any regression is an attempt to model a distribution of dependent data (here, $F_{\beta\beta}$ vs f). Therefore, removing overly influential samples is a necessary step in satisfying the prerequisites of the statistical modeling. In this sense, a sample flagged by ARIIS’s D filter may not be an outlier in the layman’s sense (i.e. false or erroneous data), but this sample *should* be removed anyway because it exerts disproportionate influence on the regression as compared with the entire distribution.

An example of the fitting algorithm is given in Fig. 4. The high correlation coefficient squared r^2 in both cases, especially the improvement after applying D_{thresh} , demonstrates that ARIIS captures a log-linear portion of the spectrum. This is critical because this statistical form is only possible if ε is independent of scale. Also,

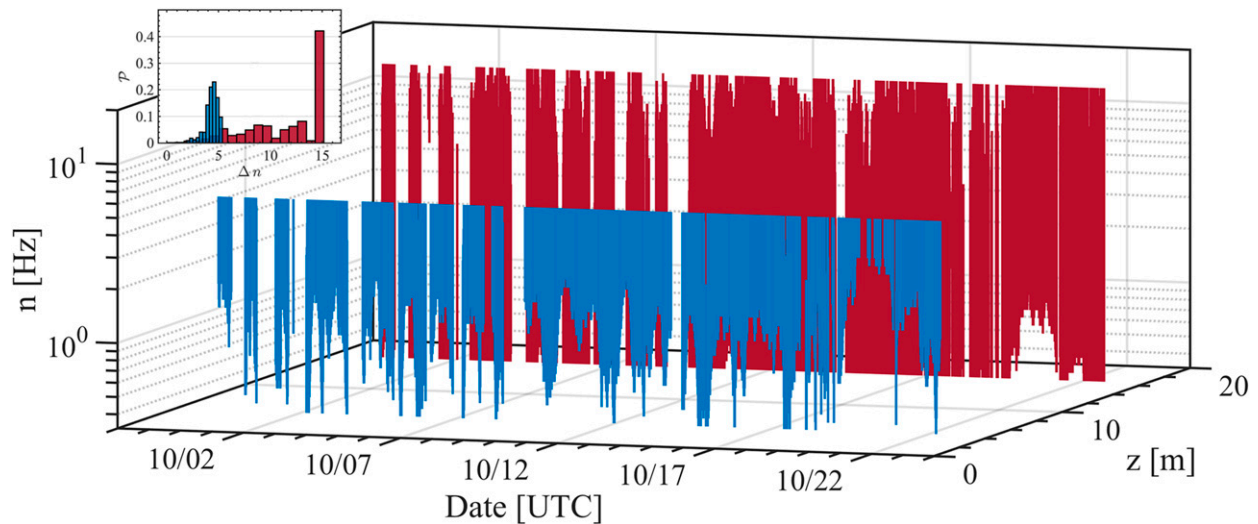


FIG. 5. Time series of the final bandwidth Δn that is output from ARIIS for the lowest (blue) and uppermost (red) flux levels. The inset shows probability distributions \mathcal{P} of Δn ; the number of bins in the histograms was held constant.

it is evident from this example that both F_{uu} and F_{ww} can be log linear and exhibit different spectral slopes (i.e., $m_{uu} \neq m_{ww}$). The total impact of all the rejection criteria executed by ARIIS as applied to the CASPER-West dataset was an average $32.9\% \pm 1.1\%$ data loss rate, across the entire profile. The overwhelming majority (96%) of spectra were rejected because of unfavorable wind directions. Therefore, making similar measurements not near a large platform or structure should improve the number of individual spectra that can be processed using this method.

5. Example results from CASPER-West

ARIIS was applied to 23 consecutive days of mast observations. As with any automatic processor, spurious or unphysical values may be included in the final dataset. These values (e.g., $m_{\beta\beta} > 0$) were flagged and removed before analysis. For any given flux level, these outliers reflect at most a few tenths of a percent of the entire distribution. Here, z refers to the global median height above the mean water level underneath *FLIP*'s boom.

a. The inertial subrange bandwidth

The variability in Δn identified by ARIIS is given in Fig. 5. To the authors' knowledge, this is the first-ever time record of the Kolmogorov inertial subrange bandwidth observed within the atmosphere. For the lowest measurement level, there was substantial variability in the low-frequency limit of the inertial subrange. It was found that Δn tended to decrease (become narrower) as U increased, which was attributed to the constraint set by U/z and the Nyquist frequency (10 Hz)

of the lowest two anemometers. When U exceeded 10 m s^{-1} , it was possible that Δn was outside the resolved frequency range, that is, no inertial subrange was detected (gaps in Fig. 5).

This degree of variability was less consistent for the upper measurement levels, which could resolve a larger range of turbulent eddy scales. In fact, for $z = 16 \text{ m}$, over 60% of all $\Delta n > 10 \text{ Hz}$, with the peak in the probability distribution being 0.42 at $\Delta n = 15 \text{ Hz}$ (see Fig. 5). This indicates that the identified subrange spanned to the low-pass filter cutoff; therefore, with a higher-resolution sensor, one would expect an even wider Δn .

It is anticipated that some properties of Δn may be related to thermal stability and wind speed. Figure 6 provides the low-frequency limit (or initiation frequency, n_i) of the ARIIS-determined Δn in both unstable ($\zeta < 0$) and stable ($\zeta > 0$) regimes, for four heights along the mast: $z = 3, 5, 12, \text{ and } 16 \text{ m}$. These frequencies are limited at the lower range by $1/3 \text{ Hz}$ (used for CASPER-West to mitigate surface gravity wave influence) and thus the low-frequency tails of these distributions collapse on this value. Figure 6 n_i increases as $|\zeta| \rightarrow 0$ and as wind speed increases. This effect was pronounced closer to the surface, where $U/z \leq n_i$ creates a physical constraint on the range of isotropic eddies that an ultrasonic anemometer can resolve (Figs. 6d,h). In the very near neutral limit ($|\zeta| < 0.001$), the n_i appears to become independent of ζ , with wind speed being the only factor controlling the inertial subrange initiation (Figs. 6b,c,g). In the cases of $z > 12 \text{ m}$ and $\zeta > 0$, n_i exhibited little dependence on either ζ or wind speed (Figs. 6e,f).

Although investigating the variability of Δn and n_i is interesting and novel, given the output of ARIIS, sonic

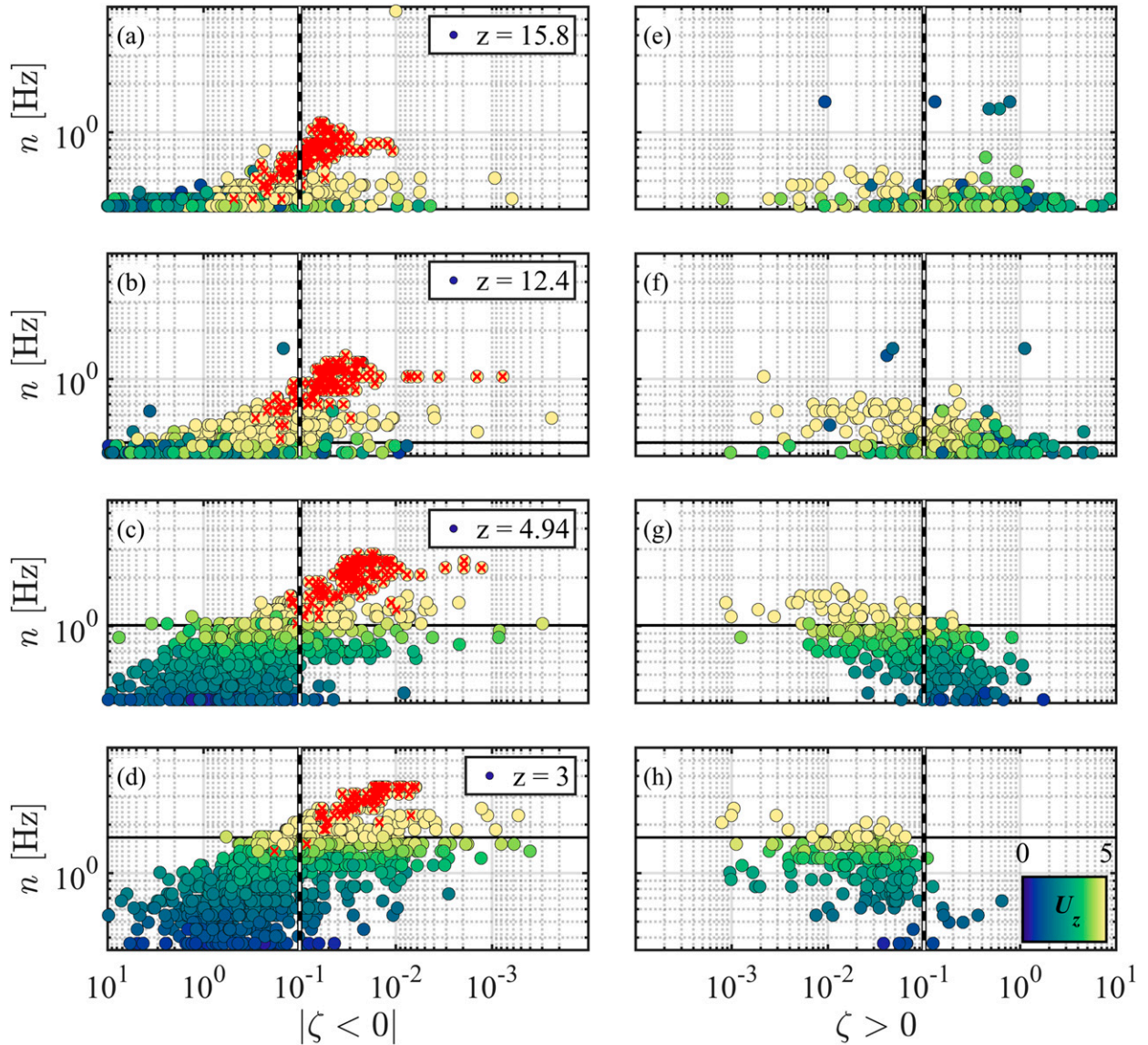


FIG. 6. The ARIIS-detected inertial subrange initiation frequency n_i as a function of ζ for (a)–(d) unstable and (e)–(h) stable conditions, with the points colored by U_z up to 5 m s^{-1} (from blue to yellow). The high-wind event (0000 UTC 20 Oct–1200 UTC 21 Oct) is marked with orange times signs. In each panel, the horizontal solid line marks the $n_i = U/z$ limit for $U_z = 5$ [in (a), (e), this line falls below the axis limits]; vertical black and white dashed lines denote $|\zeta| = 0.1$.

anemometry is not best suited for probing the frequency dependence and characteristics of the inertial subrange. Therefore, this analysis was provided as primarily qualitative, and the remainder of this article will focus on the inertial subrange slope, which should be independent of the actual Δn .

b. The inertial subrange slope

Probability distributions \mathcal{P} of normalized m_{uu} and m_{ww} revealed considerable spread in the empirically derived inertial subrange power law (Fig. 7). The μ was examined for both components, and, while there was

some uncertainty in individual estimates of the slope, this uncertainty was dominated by intersample variability. For both velocity components, \mathcal{P} were fairly Gaussian, but with a height-dependent mean and variance. In particular, for the highest flux level, the peak $\mathcal{P}(m_{\beta\beta}/m_0)$ was 1.05, which indicates a slightly steeper than expected slope over the inertial subrange. For the levels at or below 4 m, the peak $\mathcal{P}(m_{\beta\beta}/m_0)$ tended to be less than 1. This indicates a spectral slope that is substantially shallower than was predicted by Kolmogorov. Physically, this represents more energy per eddy scale over the inertial subrange. For m_{uu} , the

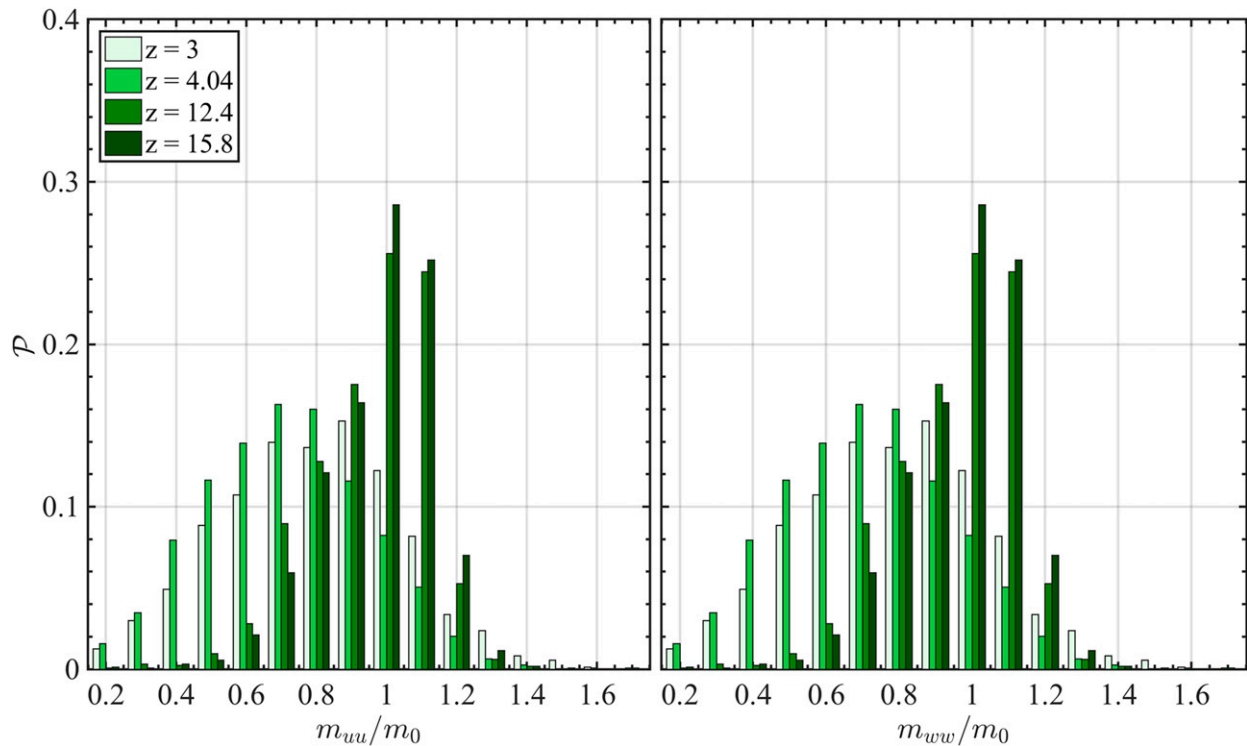


FIG. 7. Probability distributions \mathcal{P} of (left) m_{uu}/m_0 and (right) m_{ww}/m_0 for four measurement levels of the profile. A ratio of unity indicates agreement with Kolmogorov's theory.

peaks in \mathcal{P} were 0.9 and 0.7 for z at 3 and 4.04 m, respectively. However, the distributions for these levels were fairly broad even though there was only a 10% difference in the means. For the vertical wind, the peak in $\mathcal{P}(m_{ww}/m_0)$ monotonically increased from 0.5 to just under 1.2 for z from 3 to 15.8 m. For this component, there was over a 30% difference in the mean m_{ww} between $z = 3$ and 4.04 m.

For all levels and velocity components, \mathcal{P} exhibited nonnegligible spread (or uncertainty) in the actual value of the inertial subrange power law. This may be quantified using the relative error, defined here as

$$e_r = \sigma/\mu, \quad (16)$$

where σ and μ are the sample standard deviation and mean, respectively. The levels at or below 4 m exhibited an $e_r \approx 23\%–33\%$. This drops substantially for the upper flux levels, where e_r ranged from approximately 12%–17%. In general, variance for m_{uu} was higher than m_{ww} .

A time series of $m_{\beta\beta}/m_0$ revealed no distinct temporal or diurnal dependences (Fig. 8). Most of the variance in the empirically derived power law appears to be driven by mean environmental change, events, and random uncertainty. The lack of a diurnal dependence indicates that processes such as solar radiation and the diurnal wind (i.e., land-/sea-breeze cycle), both

of which had strong signals during CASPER-West, do not affect the inertial subrange. The z dependence of $m_{\beta\beta}/m_0$ was not clearly dependent on time (Fig. 8). In general, however, the variance in $m_{\beta\beta}/m_0$ was more dependent on the height above the surface, rather than the velocity component (i.e., $\beta = u$ or w).

While m_{uu} did not exhibit a strong diurnal dependence, it did show some dependence on wind forcing and the mean azimuthal wind direction (Fig. 9). In the following description, r gives the correlation coefficient between the predictors (u_*) and response (m_{uu}/m_0). Using $z = 16$ m as an example, an overall least squares linear regression revealed a negative relationship between wind forcing u_* and m_{uu}/m_0 ($r = -0.403$). However, for $u_* < 0.2$ there was significant scatter in the observations. When only considering westerly winds ($240^\circ < \theta_z < 300^\circ$), the overall variability decreases and the inverse dependence becomes more robust ($r = -0.661$). The results for the northwesterly sector ($300^\circ < \theta_z$) were interesting, where only a very slight negative dependence on forcing was observed, which was significant ($r = -0.112$; $p = 0.028$). This trend strengthens ($r = -0.352$) and steepens in the case of higher wind forcing, though this was not statistically significant ($p = 0.12$) because of low subsample size ($N = 21$).

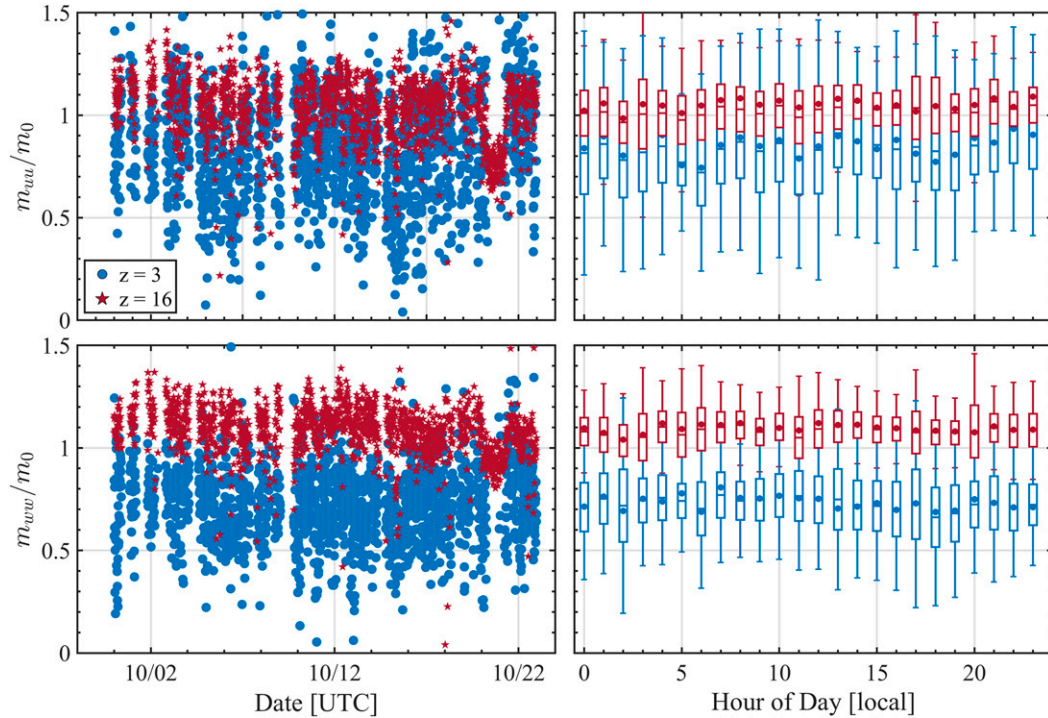


FIG. 8. (left) Time and (right) hourly dependence of (top) m_{uu}/m_0 and (bottom) m_{wv}/m_0 . The hourly dependence is given as a box-and-whisker showing the mean (centroid of box/horizontal line), median (dot), and the 50% and 95% intervals (box edges and error bars, respectively). Because of graphing limitations, some whiskers (i.e., error bars) are occluded by their boxes.

For easterly and southwesterly winds, the sample size drops to ~ 200 and no u_* values above 0.36 m s^{-1} were observed. Therefore, no significant trend with wind forcing was found. However, a two-sided Student’s t test demonstrated that m_{uu}/m_0 for easterly and southwesterly winds were significantly different ($p < 0.001$), with the former being on average 23.1% smaller than the latter. Before carrying out the test, both subsets of the data were normalized following Niaki and Abbasi (2007) to account for nonnormal distributions. Because of the relatively high sample size for these statistical tests, the Cohen’s effect size (essentially a scale-normalized t statistic) was calculated to account for the impact of sample size. The Cohen’s value was found to be 1.38, which can be considered sufficient for a significant result. Therefore, regardless of the sample size, for the southwesterly and easterly conditions, the observed differences in m_{uu}/m_0 reflect a physical change in the observed turbulence scaling as a function of the mean azimuthal wind direction.

6. Discussion

The algorithm developed here does rely on some heuristic or nonadaptive steps, such as the setting of

\mathcal{R}_c . These nonadaptive features allowed for efficient processing of a large field dataset, but they will always represent a limitation and trade-off for automatic processing. However, this highlights the fundamental issue of deciding what is “good enough” for an approximation or convergence on a theoretical value. In the MASL literature there is no standardized approach for determining convergence and confidence bounds tend to be set by the investigator. For example, Yelland and Taylor (1996) arbitrarily used $\pm 30\%$ as a cutoff for a non-Kolmogorov power law, but there are examples with 10% or 20% deviations being used. These problems are not unique to this study, or even to this field, but the analysis of these kinds of phenomena hinge on determining whether to consider a theoretical condition as being satisfied. The work presented here cannot definitively address this issue, but the results do motivate careful consideration and a standardized approach. The advantage of ARIIS, over other methods, is that it provides the information necessary for the investigator to make informed decisions about internal variability and quality of their dataset.

The CASPER-West data were used to develop ARIIS and provided an interesting opportunity for investigating the empirically derived variability of the

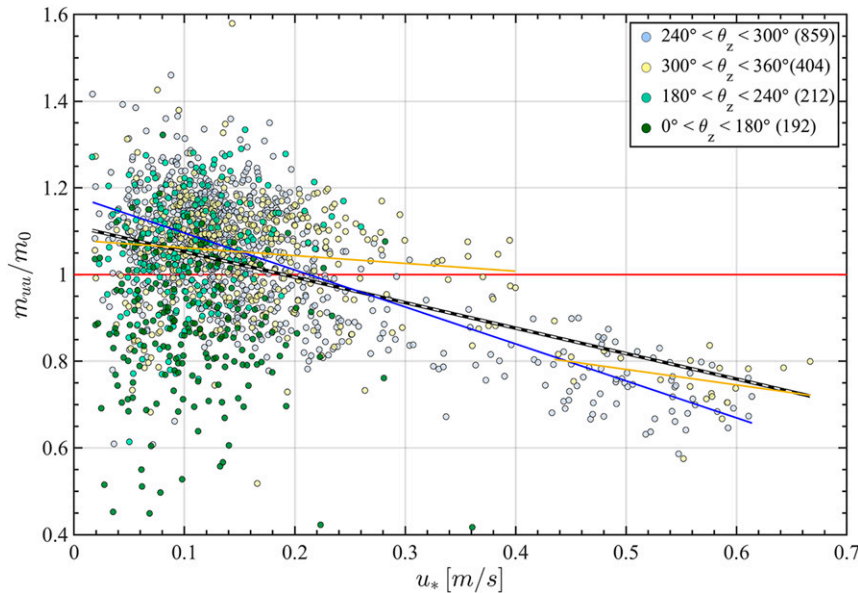


FIG. 9. Normalized m_{uu} as a function of wind forcing (u_*) segregated into different wind direction sectors θ_z for the observations from the uppermost flux level. The number of individual samples per sector is given in parentheses in the key. Linear regression lines for all observed (black and white dashed), westerly (blue), and northwesterly (gold) wind directions are shown. The red line marks $m_{uu} = m_0$.

inertial subrange slope. The results of this investigation revealed significant variance in the slope for both the along- and vertical-wind components. This variance could not be accounted for by extreme anisotropy (beyond the mean level observed), a non-log-linear spectrum over Δf , or other processing considerations. For example, the impact of varying the averaging window (Fig. 10) or FFT windowing method (Fig. 11) was evaluated. While on an individual basis, one expects differences in either the Δf or $m_{\beta\beta}$ identified, when considered in aggregate, there was no statistically significant difference in the ARIIS outcome for these different processing steps.

ARIIS was used to analyze the dependence of n_i on height above the ocean surface, wind speed, and stability, and Fig. 6 may be the first ever empirical analysis of the inertial subrange initiation frequency in a geophysical turbulent flow. The most significant limitation to this analysis was the use of ultrasonic anemometers and the proximity to ocean surface. Given their limitations at high frequencies, it was not expected that the entire subrange would be resolved for every spectrum (Chamecki and Dias 2004). Furthermore, the proximity to the ocean surface coupled with the limits of anemometry sampling frequency, meant that there were limits to resolving n_i when it became too low or too high. In theory, Δn , defined only by the $-5/3$ power law, is expected to widen from both low- and high-

frequency limits with increasing flow speed (Tennekes and Lumley 1972). However, for a fixed height within the surface layer, as the wind speed increases the low-frequency limit of the inertial subrange (i.e., $f = U/z$) moves to higher and higher frequencies, constraining Δn to a much narrower range than would be predicted by $-5/3$ alone. This demonstrates the need to account for isotropy when determining the location of the inertial subrange.

In absolute terms, the variance in $m_{\beta\beta}$ tended to be constrained within $\pm 20\%$ of the mean, which itself was approximately within 10% of m_0 . The major exceptions were for the two lowest observing levels of the FLIP mast. Therefore, as an example, the majority of these observations would have passed the Yelland and Taylor (1996) criteria. However, more detailed investigations revealed that this variance was nonrandomly distributed and revealed systematic dependence on wind forcing and direction. In the case of west to northwesterly winds, increased wind forcing was associated with slopes shallower than Kolmogorov's expected value. Also, for the same wind forcing, easterly winds exhibited significantly shallower slopes than southwesterly winds. In this region, changing wind direction will most likely affect the interaction between the turbulent flow and the underlying wave field. The intensity of the wind-generated waves correlates significantly with friction velocity (e.g., Kraus and Businger 1994),

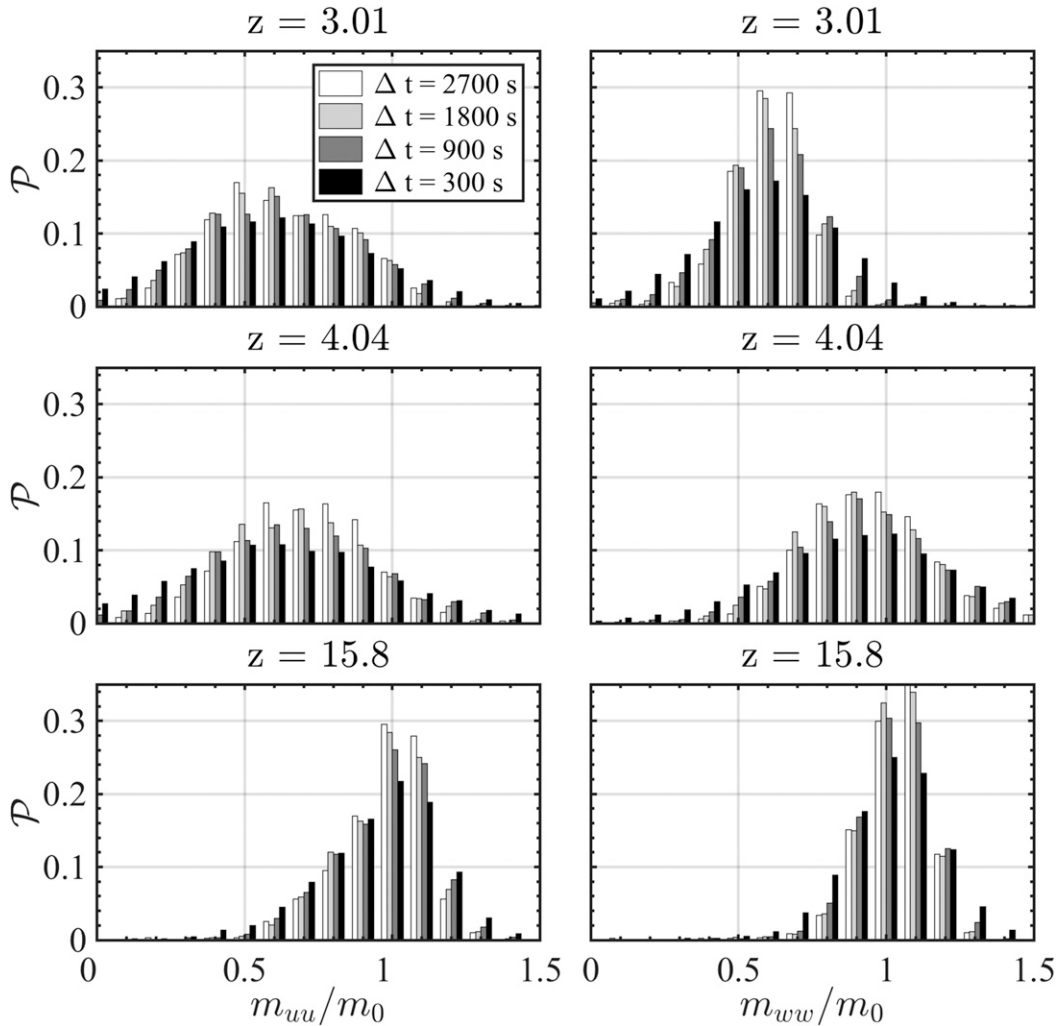


FIG. 10. The \mathcal{P} of $m_{\beta\beta}/m_0$ using four different window lengths. Note that these \mathcal{P} include some spurious output from ARIIS (less than 1% of the total distribution)—these values were filtered out of the dataset analyzed in Figs. 7–9.

and therefore, the distribution in Fig. 9 is a preliminary indication of a relationship between the inertial subrange slope and wave activity. This interaction is somewhat unexpected, given the frequency range of the inertial subrange, and more work is needed to fully understand this mechanism. While there may be some impact from changing fetch, given the coastline and islands, this work was solely focused on the high-frequency range of the wind variance spectrum, which would be expected to adjust to a changing surface roughness quickly. The closest land area was Santa Barbara Island, which was nearly 45 km from *FLIP* and has an area of ~ 2 km². The results of the analysis into the CASPER-West observations revealed significant and unexpected variability in the empirically derived inertial subrange slope; however, a full exploration of the underlying variability in the slope goes beyond

the scope of this work. This further effort is the focus of work currently under peer review for publication, as well as further investigation and study.

7. Summary

Presented here was the design and implementation of a novel approach to detecting Kolmogorov’s inertial subrange in velocity variance spectra. The novelty of ARIIS is not in the exercise, since ad hoc inertial subrange detection methods are pervasive in the literature. Rather, ARIIS lays out a series of controlled steps for analyzing a single velocity variance spectrum and identifying the most probable location of the subrange. This is executed adaptively and efficiently, which is useful for large datasets, where visual inspection imposes an onerous burden on the investigator. While ARIIS is

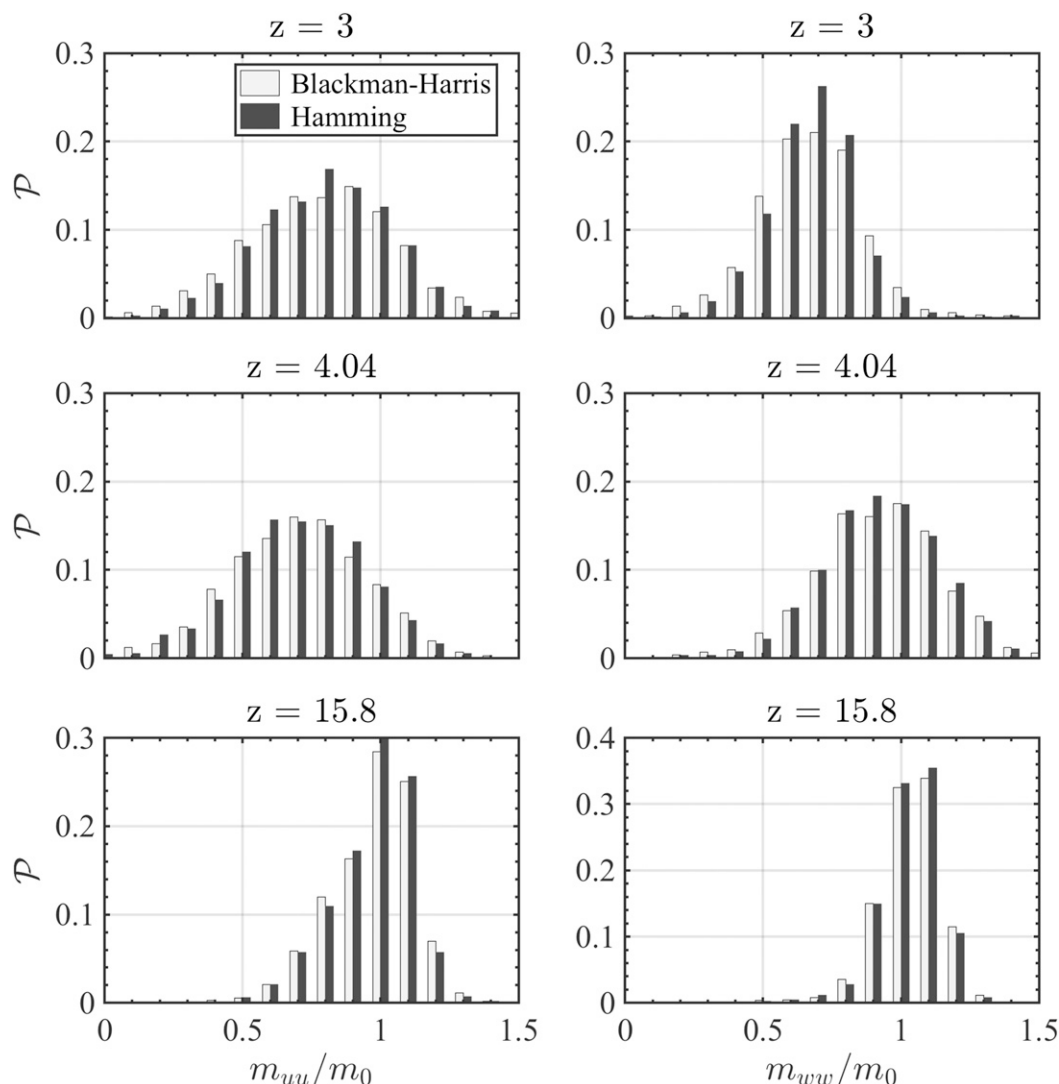


FIG. 11. As in Fig. 10, but comparing different windowing techniques. The Blackman–Harris window was used to generate the results presented here (Figs. 7–10), but the Hamming window was recommended by Kaimal and Kristensen (1991). Both windowing techniques were applied over the entire domain and applied using MATLAB’s native functions in default mode (see the MATLAB documentation).

fundamentally based on Kolmogorov’s original considerations (i.e., isotropy), the design of the program makes a concerted effort to minimize reliance on theoretical assumptions about turbulence variability. Specifically, the determination of the actual onset of the isotropic subrange and a robust measurement of the observed inertial subrange slope makes this approach novel as compared with other methods in the study of turbulence within the ASL—and in general, for turbulence cascade studies in both atmospheric and oceanic domains.

ARIIS was used to investigate the empirically derived slope in turbulence measurements made from *FLIP*. As a result of ARIIS’s novel approach, this study provided

the first analysis of the complex variability of the observed inertial subrange bandwidth and initiation frequency within the atmosphere. In addition, the findings revealed significant variability in the observed inertial subrange slope that could be attributed to both random variance as well as a systematic dependence on the mean forcing within the MASL. In particular, the slope exhibited a dependence on the mean wind forcing and the mean azimuthal wind direction. This suggests that the turbulent energy distribution within the airflow above the ocean surface is dependent on the mechanical interaction between the wind and waves and that this interaction changes with the relative velocities of these two fields. Future efforts should focus on characterizing

this physical mechanism and determining how general these findings are within the interfacial layer, in both air and water.

Acknowledgments. This research was part of the Coupled Air–Sea Processes and Electromagnetic Ducting Research project funded by the Office of Naval Research (ONR) Grant N0001418WX01087 under its Multidisciplinary University Research Initiative (MURI). This work would not have been possible without the tremendous efforts of the captain and crew of *FLIP*; their enabling of our work is greatly appreciated. Field campaigns are massive undertakings, and the success of this project must be attributed to the collective effort of the CASPER team. Of particular note are members of Qing Wang’s research group: Denny Alappattu, Alex Olson, Ben Wauer, Kyle Franklin, and Anna Hook, who helped with the field data collection portion of this work. Richard Lind (Naval Postgraduate School) is appreciated for his help in preparation for CASPER-West. We thank Campbell Scientific, Inc., for their support and responsiveness in helping us to conduct a postexperiment data quality investigation. We appreciate the efforts of three anonymous reviewers, whose efforts strengthened this work. The dataset used in this analysis is available online (<https://nps.box.com/s/dyfswo8ly0qwmgki3nmrfy06265nk0kz>), as is the ARIIS code (<https://github.com/dortizsu/ARIIS>).

REFERENCES

- Anderson, R., 1993: A study of wind stress and heat flux over the open ocean by the inertial-dissipation method. *J. Phys. Oceanogr.*, **23**, 2153–2161, [https://doi.org/10.1175/1520-0485\(1993\)023<2153:ASOWSA>2.0.CO;2](https://doi.org/10.1175/1520-0485(1993)023<2153:ASOWSA>2.0.CO;2).
- Atta, C. W. V., and W. Y. Chen, 1970: Structure functions of turbulence in the atmospheric boundary layer over the ocean. *J. Fluid Mech.*, **44**, 145–159, <https://doi.org/10.1017/S002211207000174X>.
- Babić, K., and M. W. Rotach, 2018: Turbulence kinetic energy budget in the stable boundary layer over a heterogeneous surface. *Quart. J. Roy. Meteor. Soc.*, **144**, 1045–1062, <https://doi.org/10.1002/qj.3274>.
- Batchelor, G. K., 1947: Kolmogoroff’s theory of locally isotropic turbulence. *Math. Proc. Cambridge Philos. Soc.*, **43**, 533–559, <https://doi.org/10.1017/S0305004100023793>.
- , 1953: The universal equilibrium theory. *The Theory of Homogeneous Turbulence*, Cambridge University Press, 103–132.
- Chamecki, M., and N. L. Dias, 2004: The local isotropy hypothesis and the turbulent kinetic energy dissipation rate in the atmospheric surface layer. *Quart. J. Roy. Meteor. Soc.*, **130**, 2733–2752, <https://doi.org/10.1256/qj.03.155>.
- Chatterjee, S., and A. S. Hadi, 1988: Influential observations, high leverage points, and outliers in linear regression. *Stat. Sci.*, **1**, 379–393.
- Deacon, E. L., 1988: The streamwise Kolmogoroff constant. *Bound.-Layer Meteor.*, **42**, 9–17, <https://doi.org/10.1007/BF00119871>.
- Durand, P., L. De Sa, A. Druihlet, and F. Said, 1991: Use of the inertial dissipation method for calculating turbulent fluxes from low-level airborne measurements. *J. Atmos. Oceanic Technol.*, **8**, 78–84, [https://doi.org/10.1175/1520-0426\(1991\)008<0078:UOTIDM>2.0.CO;2](https://doi.org/10.1175/1520-0426(1991)008<0078:UOTIDM>2.0.CO;2).
- Edson, J. B., and C. W. Fairall, 1998: Similarity relationships in the marine atmospheric surface layer for terms in the TKE and scalar variance budgets. *J. Atmos. Sci.*, **55**, 2311–2328, [https://doi.org/10.1175/1520-0469\(1998\)055<2311:SRITMA>2.0.CO;2](https://doi.org/10.1175/1520-0469(1998)055<2311:SRITMA>2.0.CO;2).
- , —, P. G. Mestayer, and S. E. Larsen, 1991: A study of the inertial-dissipation method for computing air–sea fluxes. *J. Geophys. Res.*, **96**, 10 689–10 711, <https://doi.org/10.1029/91JC00886>.
- , A. A. Hinton, K. E. Prada, J. E. Hare, and C. W. Fairall, 1998: Direct covariance flux estimates from mobile platforms at sea. *J. Atmos. Oceanic Technol.*, **15**, 547–562, [https://doi.org/10.1175/1520-0426\(1998\)015<0547:DCFEFM>2.0.CO;2](https://doi.org/10.1175/1520-0426(1998)015<0547:DCFEFM>2.0.CO;2).
- , and Coauthors, 2013: On the exchange of momentum over the open ocean. *J. Phys. Oceanogr.*, **43**, 1589–1610, <https://doi.org/10.1175/JPO-D-12-0173.1>.
- Fairall, C. W., and S. E. Larsen, 1986: Inertial-dissipation methods and turbulent fluxes at the air–ocean interface. *Bound.-Layer Meteor.*, **34**, 287–301, <https://doi.org/10.1007/BF00122383>.
- Fisher, F. H., and F. N. Spiess, 1963: *FLIP—Floating Instrument Platform*. *J. Acoust. Soc. Amer.*, **35**, 1633–1644, <https://doi.org/10.1121/1.1918772>.
- Grachev, A. A., E. L. Andreas, C. W. Fairall, P. S. Guest, and P. Persson, 2015: Similarity theory based on the Dougherty–Ozmidov length scale. *Quart. J. Roy. Meteor. Soc.*, **141**, 1845–1856, <https://doi.org/10.1002/qj.2488>.
- Hackerott, J. A., M. B. Paskyabi, S. T. Kral, J. Reuder, A. P. De Oliveira, E. P. M. Filho, M. D. S. Mesquita, and R. De Camargo, 2016: Similarity analysis of turbulent transport and dissipation for momentum, temperature, moisture, and CO₂ during BLLAST. *Atmos. Chem. Phys. Discuss.*, <https://doi.org/10.5194/acp-2015-1061>.
- , —, J. Reuder, A. de Oliveira, S. T. Kral, E. P. Marques Filho, M. S. Mesquita, and R. de Camargo, 2017: A surface-layer study of the transport and dissipation of turbulent kinetic energy and the variances of temperature, humidity and CO₂. *Bound.-Layer Meteor.*, **165**, 211–231, <https://doi.org/10.1007/s10546-017-0271-0>.
- Hogstrom, U., 1996: Review of some basic characteristics of the atmospheric surface layer. *Bound.-Layer Meteor.*, **78**, 215–246, <https://doi.org/10.1007/BF00120937>.
- Jabbari, A., L. Boegman, and U. Piomelli, 2015: Evaluation of the inertial dissipation method within boundary layers using numerical simulations. *Geophys. Res. Lett.*, **42**, 1504–1511, <https://doi.org/10.1002/2015GL063147>.
- Jimenez, J., A. A. Wray, P. G. Saffman, and R. S. Rogallo, 1992: The structure of intense vorticity in homogeneous isotropic turbulence. *J. Fluid Mech.*, **255**, 65–90, <https://doi.org/10.1017/S0022112093002393>.
- Kaimal, J. C., 1978: Horizontal velocity spectra in an unstable surface layer. *J. Atmos. Sci.*, **35**, 18–24, [https://doi.org/10.1175/1520-0469\(1978\)035<0018:HVSIAU>2.0.CO;2](https://doi.org/10.1175/1520-0469(1978)035<0018:HVSIAU>2.0.CO;2).
- , and L. Kristensen, 1991: Time series tapering for short data samples. *Bound.-Layer Meteor.*, **57**, 187–194, <https://doi.org/10.1007/BF00119719>.
- , J. Wyngaard, Y. Izumi, and O. Cote, 1972: Spectral characteristics of surface-layer turbulence. *Quart. J. Roy. Meteor. Soc.*, **98**, 563–589, <https://doi.org/10.1002/qj.49709841707>.

- Kolmogorov, A., 1941a: Dissipation of energy in locally isotropic turbulence. *Dokl. Akad. Nauk SSSR*, **32**, 16–18.
- , 1941b: The local structure of turbulence in incompressible viscous fluid for very large Reynolds numbers. *Dokl. Akad. Nauk SSSR*, **30**, 301–305.
- Kraus, E., and J. Businger, 1994: *Atmosphere–Ocean Interaction*. Oxford University Press, 362 pp.
- Large, W. G., and S. Pond, 1981: Open ocean momentum flux measurements in moderate to strong winds. *J. Phys. Oceanogr.*, **11**, 324–336, [https://doi.org/10.1175/1520-0485\(1981\)011<0324:OOMFMI>2.0.CO;2](https://doi.org/10.1175/1520-0485(1981)011<0324:OOMFMI>2.0.CO;2).
- , and —, 1982: Sensible and latent heat flux measurements over the ocean. *J. Phys. Oceanogr.*, **12**, 464–482, [https://doi.org/10.1175/1520-0485\(1982\)012<0464:SALHFM>2.0.CO;2](https://doi.org/10.1175/1520-0485(1982)012<0464:SALHFM>2.0.CO;2).
- MacCready, P., 1962: The inertial subrange of atmospheric turbulence. *J. Geophys. Res.*, **67**, 1051–1059, <https://doi.org/10.1029/JZ067i003p01051>.
- Miyake, M., R. W. Stewart, and R. W. Burling, 1970: Spectra and cospectra of turbulence over water. *Quart. J. Roy. Meteor. Soc.*, **96**, 138–143, <https://doi.org/10.1002/qj.49709640714>.
- Muñoz-Esparza, D., R. D. Sharman, and J. K. Lundquist, 2018: Turbulence dissipation rate in the atmospheric boundary layer: Observations and WRF mesoscale modeling during the XPIA field campaign. *Mon. Wea. Rev.*, **146**, 351–371, <https://doi.org/10.1175/MWR-D-17-0186.1>.
- Niaki, S. T. A., and B. Abbasi, 2007: Skewness reduction approach in multi-attribute process monitoring. *Commun. Stat. Theory Methods*, **36**, 2313–2325, <https://doi.org/10.1080/03610920701215456>.
- Onsager, L., 1945: The distribution of energy in turbulence. *Phys. Rev.*, **68**, 286.
- Ortiz-Suslow, D. G., J. Kalogiros, R. Yamaguchi, D. Alappattu, K. Franklin, B. Wauer, and Q. Wang, 2019: The data processing and quality control of the marine atmospheric boundary layer measurement systems deployed by the Naval Postgraduate School during the CASPER-West field campaign. Naval Postgraduate School Tech. Rep. NPS-MR-19-001, 98 pp., <https://calhoun.nps.edu/handle/10945/61638>.
- Payne, F. R., and J. L. Lumley, 1966: One-dimensional spectra derived from an airborne hot-wire anemometer. *Quart. J. Roy. Meteor. Soc.*, **92**, 397–401, <https://doi.org/10.1002/qj.49709239309>.
- Sjöblom, A., and A. Smedman, 2002: The turbulent kinetic energy budget in the marine atmospheric surface layer. *J. Geophys. Res.*, **107**, 3142, <https://doi.org/10.1029/2001JC001016>.
- Starkenbug, D., S. Metzger, G. J. Fochesatto, J. G. Alfieri, R. Gens, A. Prakash, and J. Cristóbal, 2016: Assessment of despiking methods for turbulence data in micrometeorology. *J. Atmos. Oceanic Technol.*, **33**, 2001–2013, <https://doi.org/10.1175/JTECH-D-15-0154.1>.
- Tennekes, H., and J. Lumley, 1972: *A First Course in Turbulence*. MIT Press, 300 pp.
- Wang, Q., and Coauthors, 2018: CASPER: Coupled Air–Sea Processes and Electromagnetic Ducting Research. *Bull. Amer. Meteor. Soc.*, **99**, 1449–1471, <https://doi.org/10.1175/BAMS-D-16-0046.1>.
- Wyngaard, J. C., 2010: *Turbulence in the Atmosphere*. Cambridge University Press, 387 pp.
- , and S. F. Clifford, 1977: Taylor’s hypothesis and high-frequency turbulence spectra. *J. Atmos. Sci.*, **34**, 922–929, [https://doi.org/10.1175/1520-0469\(1977\)034<0922:THAHTS>2.0.CO;2](https://doi.org/10.1175/1520-0469(1977)034<0922:THAHTS>2.0.CO;2).
- Yaglom, M., 1981: Laws of small scale turbulence in atmosphere and ocean (in commemoration of the 40th anniversary of the theory of locally isotropic turbulence). *Izv. Atmos. Ocean. Phys.*, **17**, 1235–1257.
- Yelland, M., and P. K. Taylor, 1996: Wind stress measurements from the open ocean. *J. Phys. Oceanogr.*, **26**, 541–558, [https://doi.org/10.1175/1520-0485\(1996\)026<0541:WSMFTO>2.0.CO;2](https://doi.org/10.1175/1520-0485(1996)026<0541:WSMFTO>2.0.CO;2).
- Yeung, P. K., and Y. Zhou, 1997: Universality of the Kolmogorov constant in numerical simulations of turbulence. *Phys. Rev.*, **56E**, 1746–1752, <https://doi.org/10.1103/PhysRevE.56.1746>.